

CARRINGTON MAPS OF Ca II K-LINE EMISSION FOR THE YEARS 1915–1985

N. R. SHEELEY, JR., T. J. COOPER¹, AND J. R. L. ANDERSON²
Space Science Division, Naval Research Laboratory, Washington, DC 20375-5352, USA; neil.sheeley@nrl.navy.mil
Received 2010 December 3; accepted 2011 January 22; published 2011 March 3

ABSTRACT

We have used Mount Wilson Observatory calcium K-line images, digitized and flat fielded by the solar group at UCLA, to construct Carrington maps of Ca II 3934 Å intensity for the years 1915–1985. These maps have a spatial resolution comparable to the resolution of Carrington maps of the magnetic field observed at Kitt Peak and a spectral resolution comparable to the width of the K₂₃₂ emission. Consequently, they provide a way of tracking the spatial distribution of magnetic flux from the present back to the year 1915. In this paper, we compare some of the recent K-line maps with corresponding maps of magnetic field, and show examples of K-line maps during earlier sunspot cycles when high-quality magnetograms were not available. Then, we use butterfly diagrams and super-synoptic displays to summarize the long-term evolution of the patterns of calcium intensity. Although each cycle has characteristics that are similar to the others, cycle 19 is remarkable for its broad latitudinal distribution of active regions, for its giant poleward surges of flux, and for the emergence of a north–south asymmetry that lasted 10 years.

Key words: Sun: chromosphere – Sun: faculae, plages – Sun: filaments, prominences – Sun: surface magnetism

1. INTRODUCTION

The Sun has just emerged from the longest and deepest sunspot minimum in living memory. (See Cranmer et al. 2010, and papers contained therein.) Nine sunspot cycles have passed since the last extended minimum in 1913, and five cycles have passed since the second weakest minimum in 1954. Thus, the recent sunspot minimum during 2008–2009 was a quiet reminder that all sunspot cycles are not the same and that historical observations may provide insight into the operation of the sunspot cycle.

Motivated by this reminder, we have used the archive of daily Ca II K-line spectroheliograms, digitized and flat fielded by the solar physics group at UCLA (Lefebvre et al. 2005; Bertello et al. 2010), to construct Carrington maps of K-line intensity, spanning the 70 year interval 1915–1985. Detailed descriptions of the individual K-line images are given on the Web site of the Mount Wilson Solar Photographic Archive Digitization Project³ and in the recent papers of Ermolli et al. (2009) and Foukal et al. (2009). In addition, detailed descriptions of the spectroheliograph are given by Ellerman (1919) for the initial years of operation and by Title (1966) for the mid-1960s.

Because the enhanced K₂₃₂ emission is closely related to the occurrence of magnetic fields (Leighton 1959), we expect these Carrington maps to indicate the magnetic flux distribution during prior sunspot cycles when magnetograms were not available. Consequently, the maps may be useful for constraining models of magnetic flux transport on the surface of the Sun during multiple sunspot cycles (Wang et al. 2002; Schrijver et al. 2002; Mackay 2003; Baumann et al. 2004; Jiang et al. 2010), or flux-transport models of the solar dynamo (Wang et al. 1991; Choudhuri et al. 1995; Küker et al. 2001; Charbonneau 2005; Dikpati 2005; Dikpati & Gilman 2009; Muñoz-Jaramillo et al. 2010; Karak 2010). In addition, the maps may be useful for estimating the long-term contribution of facula emission to the total solar irradiance (Foukal & Lean 1988; Lean et al. 1998; Krivova et al. 2007; Lean 2010).

After describing our map-making procedure, we illustrate the quality of the resulting maps by comparing a relatively clean calcium map during Carrington rotation 1683 (1979 June 19–July 16) with the corresponding map of photospheric magnetic field obtained at Kitt Peak. Then, working backward from the present, we show examples of maps obtained during earlier times and summarize the entire data set in butterfly diagrams of the longitudinally averaged intensity and in so-called super-synoptic displays (Ulrich et al. 2002). As we shall see, cycle 19 stands out for its wide belts of solar activity, for its giant poleward surges of flux, and for the north–south asymmetry that emerged just after sunspot maximum and persisted until the peak of cycle 20.

2. THE MAP-MAKING PROCEDURE

We generated Carrington maps of Ca II K-line intensity in the traditional manner described by Harvey & Worden (1998) and Ulrich & Boyden (2006) for Carrington maps of photospheric magnetic field. In particular, we cropped each daily image along meridians within 60° from the central meridian; we transformed the cropped images to a rectangular (longitude, sine latitude) coordinate system (correcting for the effect of the apparent tilt, B_0 , of the Sun’s rotational axis, but ignoring the 0.5 variation between the lines of sight to different points on the Sun’s disk).

We deposited these daily “minimaps” into the Carrington grid using a $\cos^4(\phi - \phi_0)$ weighting that favors the central meridian, ϕ_0 , over more remote longitudes, ϕ , up to the 60° limit. The 60° limit was a compromise between spatial resolution and data continuity; smaller limits produced less spatial blurring, but more data gaps. The maps were not sensitive to the amount of weighting; we chose the fourth power simply to match the weighting used for the National Solar Observatory (NSO) magnetograms (Harvey & Worden 1998). It was necessary to remove the streaks that resulted from superimposing these minimaps, but this was relatively easy to do. We simply divided the Carrington map by a “streak map,” obtained by setting the intensities of the individual K-line images equal to unity before applying the map-making procedure.

¹ Now at Cornell University, Ithaca, NY 14853, USA.

² Now at Princeton University, Princeton, NJ 08544, USA.

³ http://ulrich.astro.ucla.edu/MW_SPADP/index.html

Report Documentation Page			Form Approved OMB No. 0704-0188		
<p>Public reporting burden for the collection of information is estimated to average 1 hour per response, including the time for reviewing instructions, searching existing data sources, gathering and maintaining the data needed, and completing and reviewing the collection of information. Send comments regarding this burden estimate or any other aspect of this collection of information, including suggestions for reducing this burden, to Washington Headquarters Services, Directorate for Information Operations and Reports, 1215 Jefferson Davis Highway, Suite 1204, Arlington VA 22202-4302. Respondents should be aware that notwithstanding any other provision of law, no person shall be subject to a penalty for failing to comply with a collection of information if it does not display a currently valid OMB control number.</p>					
1. REPORT DATE 03 MAR 2011	2. REPORT TYPE	3. DATES COVERED 00-00-2011 to 00-00-2011			
4. TITLE AND SUBTITLE Carrington Maps Of Ca II K-Line Emission For The Years 1915-1985					
5a. CONTRACT NUMBER 5b. GRANT NUMBER 5c. PROGRAM ELEMENT NUMBER					
6. AUTHOR(S) 5d. PROJECT NUMBER 5e. TASK NUMBER 5f. WORK UNIT NUMBER					
7. PERFORMING ORGANIZATION NAME(S) AND ADDRESS(ES) Naval Research Laboratory, Space Science Division, Washington, DC, 20375- 8. PERFORMING ORGANIZATION REPORT NUMBER					
9. SPONSORING/MONITORING AGENCY NAME(S) AND ADDRESS(ES) 10. SPONSOR/MONITOR'S ACRONYM(S)					
11. SPONSOR/MONITOR'S REPORT NUMBER(S)					
12. DISTRIBUTION/AVAILABILITY STATEMENT Approved for public release; distribution unlimited					
13. SUPPLEMENTARY NOTES The Astrophysical Journal, 730:51 (17pp), 2011 March 20					
14. ABSTRACT <p>We have used Mount Wilson Observatory calcium K-line images, digitized and flat fielded by the solar group at UCLA, to construct Carrington maps of Ca ii 3934 ?intensity for the years 1915?1985. These maps have a spatial resolution comparable to the resolution of Carrington maps of the magnetic field observed at Kitt Peak and a spectral resolution comparable to the width of the K232 emission. Consequently, they provide a way of tracking the spatial distribution of magnetic flux from the present back to the year 1915. In this paper, we compare some of the recent K-line maps with corresponding maps of magnetic field, and show examples of K-line maps during earlier sunspot cycles when high-quality magnetograms were not available. Then, we use butterfly diagrams and super-synoptic displays to summarize the long-term evolution of the patterns of calcium intensity. Although each cycle has characteristics that are similar to the others, cycle 19 is remarkable for its broad latitudinal distribution of active regions, for its giant poleward surges of flux, and for the emergence of a north?south asymmetry that lasted 10 years.</p>					
15. SUBJECT TERMS					
16. SECURITY CLASSIFICATION OF:			17. LIMITATION OF ABSTRACT Same as Report (SAR)	18. NUMBER OF PAGES 17	19a. NAME OF RESPONSIBLE PERSON
a. REPORT unclassified	b. ABSTRACT unclassified	c. THIS PAGE unclassified			

We did not attempt to calibrate the images. Instead, we made histograms of each image and normalized the “intensity” to the background value, taken to be the most commonly occurring value in the distribution (i.e., the mode). Also, we allowed for slight variations in image size by normalizing to the total number of pixels in the image. Because each fits file contained a rectangular array, we masked each image by setting the intensity of the array equal to zero outside the nearly circular solar disk before calculating the histograms and normalizing to the total number of pixels. This meant obtaining the coordinates of the center of the disk from the header and sometimes changing those coordinates before trimming the image.

We did not use all of the images, but instead chose the best image for each day. We did this for each month, occasionally recentering the image within our circular blackout mask when it was off center. Even when the best image was unsuitable for the Carrington map, we still retained it temporarily on the chance that it might fill in a large data gap and thereby permit the calculation of an otherwise indeterminate roll angle or the identification of an incorrectly marked image. Then, we rejected it before making the final map.

Next, we determined the orientations of these images relative to solar north (i.e., we measured the roll angles). We did this for all of the images obtained during 1915–1985 regardless of whether their headers contained roll information or whether the images had pole markers superimposed on them. When roll angles were available in the headers, our determinations usually agreed with them within 1° – 2° . However, even during these times, our measurements invariably revealed one or two discrepancies during each rotation. The discrepancies were due to a variety of causes including incorrect roll angles in the headers or incorrect roll calculations caused by images that were out of order, mislabeled, or upside down. So, this procedure not only corrected roll errors, but also corrected other human errors that would have adversely affected the Carrington maps. As documented below, such errors were present in only a few percent of the individual calcium images, but this translates to almost every Carrington map when one selects images in 38 day sequences for the map construction.

We took several steps to make the maps. First, we cross-correlated consecutive images in each Carrington rotation (plus the contributing images that occurred five days beyond each end of the rotation). This was a time-consuming calculation that we ran in batch mode when rolls were desired for several rotations. Next, we examined the calculated rolls for discrepancies between the values obtained when each image was correlated with the previous and following image. Such discrepancies revealed a variety of problems such as images that had wrong dates, wrong parities, non-circular shapes, different sizes, or images that were isolated by long data gaps. If we were able to fix the problem, we repeated the cross-correlation visually by blinking the consecutive rectangular minimaps on the computer screen and adjusting trial roll angles until the individual solar features coincided or shifted east–west along the screen. This process was efficient for catching images whose header dates or times were wrong and it provided an estimate of the discrepancy between our roll-angle measurements and the header values.

The next step was to display the entire sequence of images in a time-lapse movie. This helped to determine whether the images were in order with the proper rolls. Also, it provided a useful way of excluding unwanted images from the Carrington map. Such unwanted images included cosmetically flawed images, images with streaks caused by clouds, images that were so far

off the line center that they did not show faculae, and images that lacked contrast due to poor seeing or improper flat fielding. This exclusion process was subjective; we occasionally retained a slightly flawed image if it filled in a large data gap in the resulting Carrington map without degrading the map too much. Finally, we excluded the pole markers by replacing sufficiently dark features near the poles with neutral gray. Occasionally, we had to adjust the darkness threshold to avoid removing segments of polar crown filaments from the map.

The result was a collection of data files that we saved for future use. The Carrington maps were stored in 928 fits files and the corresponding roll angles were placed in separate data files. For the original flat-fielded images, we reproduced the file structure that we found in the MWO archive, listed by year and month. However, within each of these monthly directories, we created two subdirectories—a “good” subdirectory containing all of the images that we used in the map construction and a “bad” subdirectory containing the images that we rejected. The reasons for the rejection included cosmetic and instrumental defects as well as the human errors mentioned above, including images with unknown dates and images that were upside down.

At the time of this writing, the “good” directories contain 15,086 images and the “bad” directories contain 530 images. This means that we rejected about 3% of the images that we had initially selected as the best ones for each day. Some of the files in the “good” directories have suffixes added to their names, indicating that those images had problems that we were able to fix. They include 99 images with new dates, 90 images that were recentered, and 1014 images during 1980–1985 that had to be reversed because they were upside down. (Initially, we simply rejected images that were upside down because they occurred only about 1% of the time or less. However, toward the end of the project, we discovered that all of the files during 1980–1985 were systematically upside down, and therefore wrote software to reverse them.)

We started the map-making procedure in mid July 2010. By the end of the first week of September, we had constructed all of the maps for the interval 1915–1979. It took two more weeks for one of us (N.R.S.) to make the maps for the interval 1980–1985—one week to reverse all of the images (which were systematically upside down) and then to make the maps for these corrected images, and another week to discover and correct a systematic 8 hr time shift, associated with the time difference between Mount Wilson and Greenwich. The result of this 9 week activity was a directory of 928 Carrington maps spanning the years 1915–1985. Only nine Carrington rotations (1140, 1147–1151, 1210, 1726, and 1756) were left out. In addition, we produced 928 tables of measured roll angles and the accompanying software. Together, the roll angles and software allow one to easily remake the Carrington maps using other input parameters (such as minimap size, longitudinal weighting, spatial resolution, or alternate ways of allowing for differential rotation or for the slightly non-parallel lines of sight to different parts of the solar disk). In addition, some of the Carrington maps still contain defects that we may be able to remove (without introducing data gaps) by excluding additional cloud-streaked images. We are planning to make this material available to the solar community as part of the Mount Wilson Solar Photographic Archive Digitization Project.

3. A SAMPLE OF MAPS

Figure 1 compares a Carrington map of Ca II K-line intensity with a Carrington map of photospheric magnetic field obtained

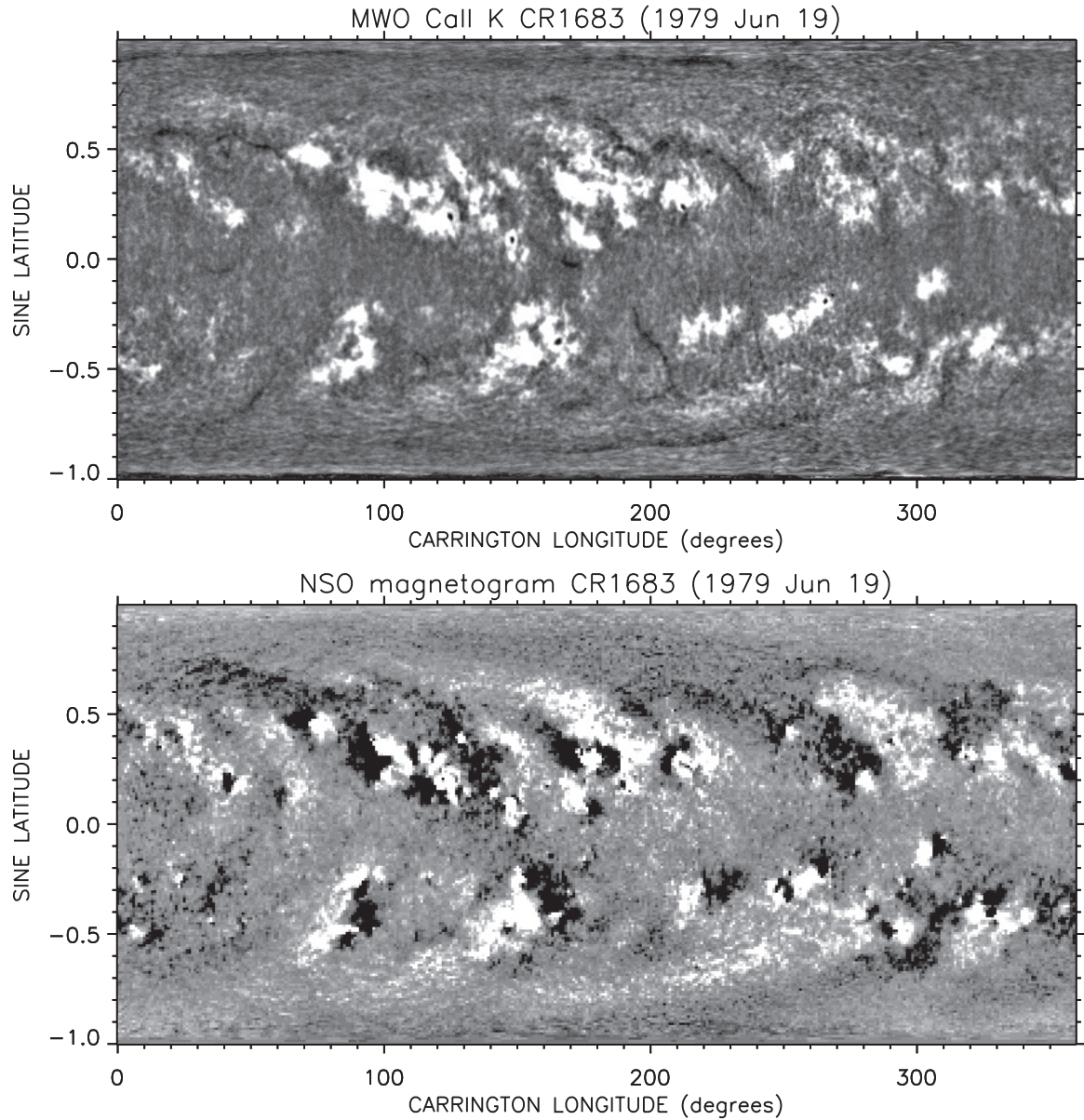


Figure 1. Carrington maps of Ca II K-line intensity (top) and NSO magnetic field (bottom) during rotation 1683, showing the close agreement between the patterns of chromospheric emission and photospheric magnetic field. In the calcium map, disk filaments separate some regions of oppositely directed magnetic field.

at Kitt Peak during rotation 1683 (starting date 1979 June 19). This was late in the rising phase of sunspot cycle 21 when large regions of trailing polarity were migrating poleward in each hemisphere. In the K-line map, these regions are separated from neighboring regions of opposite polarity by dark filaments. In particular, the lines of east–west oriented filaments at high latitude indicate that the polar fields had not yet reversed at this time.

Also, some dark sunspots are visible in the K-line map. If such photospheric features are large enough, they are sometimes visible through the K_3 chromosphere, as we have seen previously in especially high-quality Kitt Peak spectroheliograms obtained with a bandpass of 0.09 Å (Shine 1973; Bailey & Sheeley 1969). This may be why the sunspots are visible in the Carrington map for rotation 1683. However, in general, we observed many images in which sunspots were visible because the bandpass was too wide or because the exit slit was inadvertently placed too far from the line core. This was especially true during the early

years (cycles 15–17) when the spectral bandpass was broad, but it was not limited to those years. Because we were not always able to exclude such “photospheric” images from our map construction (without producing unwanted data gaps), they are a source of sunspot visibility in many of the Carrington maps.

Figure 2 provides a similar comparison for Carrington rotation 1417 (starting date 1959 August 8), which occurred toward the end of the largest sunspot maximum in modern history. We obtained the Carrington map of magnetic field from the Mount Wilson Atlas of Solar Magnetic Fields for the years 1959–1966 (Howard et al. 1967). (A black and white version of this map is also given in Figure 1 of Bumba & Howard 1965.) During this time, a large region of negative (red), trailing-polarity flux was migrating poleward from the northern-hemisphere sunspot belts to strengthen the new polar field. In contrast, the southern hemisphere showed much less activity, especially above 40° latitude (indicated by the faint horizontal line at a sine latitude of -0.64). This was not an artifact of the old magnetograms;

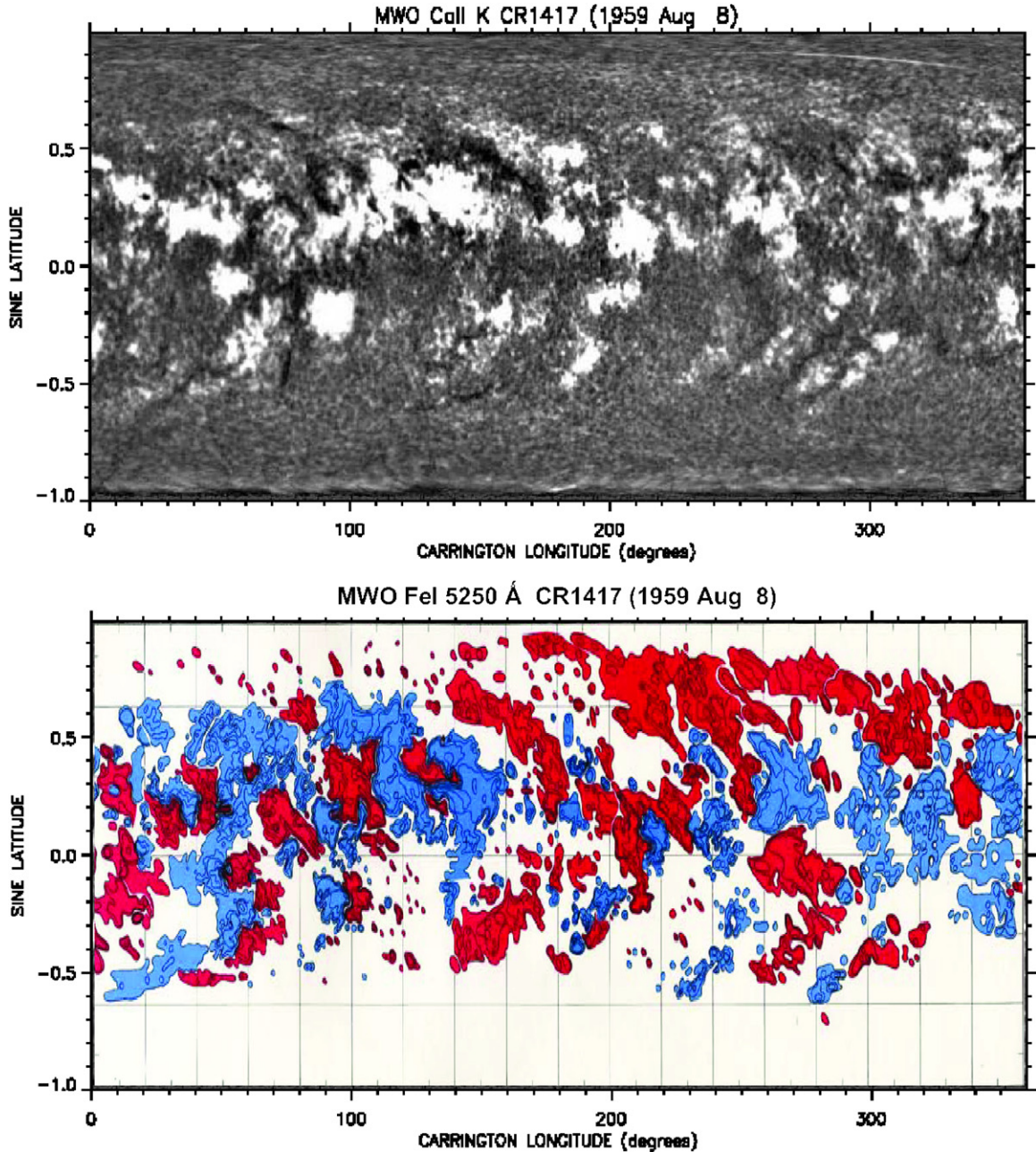


Figure 2. Carrington maps of K-line intensity (top) and MWO magnetic field from Howard et al. (1967) (bottom) during rotation 1417, showing a stream of trailing-polarity flux in the northern hemisphere and a pronounced lack of such flux at high latitudes in the southern hemisphere. In the magnetogram, blue refers to positive polarity and red refers to negative polarity.

a corresponding reduction of K-line emission is also present in the calcium map.

This north–south asymmetry was also present in Carrington rotation 1419 (starting date 1959 October 2), shown in Figure 3. At this time, the trailing-polarity region extended across the northern hemisphere (except for a data gap east of 75° longitude). It is the largest poleward surge that we have seen in all of the K-line maps going back to the year 1915.

The north–south asymmetry continued through sunspot minimum in 1964 and was present until the end of 1969 (White & Trotter 1977). In Figure 4, the Carrington maps for rotation 1508 (starting date 1966 May 25) and 1514 (starting date 1966 November 5) show this asymmetry two years after sunspot minimum. In addition to the asymmetry, one can see segments of

an east–west oriented disk filament poleward of the northern-hemisphere active regions. As we shall see later, this filament gradually migrated to the north pole and disappeared there in the first half of 1967.

Figure 5 shows that this asymmetry was also visible in the High Altitude Observatory eclipse image on November 12 (Newkirk et al. 1968). In the southern hemisphere, the corona still had its sunspot minimum configuration, dominated by the south polar coronal hole. This dominance of the south polar coronal hole occurred in spite of the relatively small number of south polar faculae (and therefore weak south polar field) during this time (Sheeley 2008).

According to Babcock (1959), the Sun's north and south polar fields weakened in 1957 and then went their separate ways.

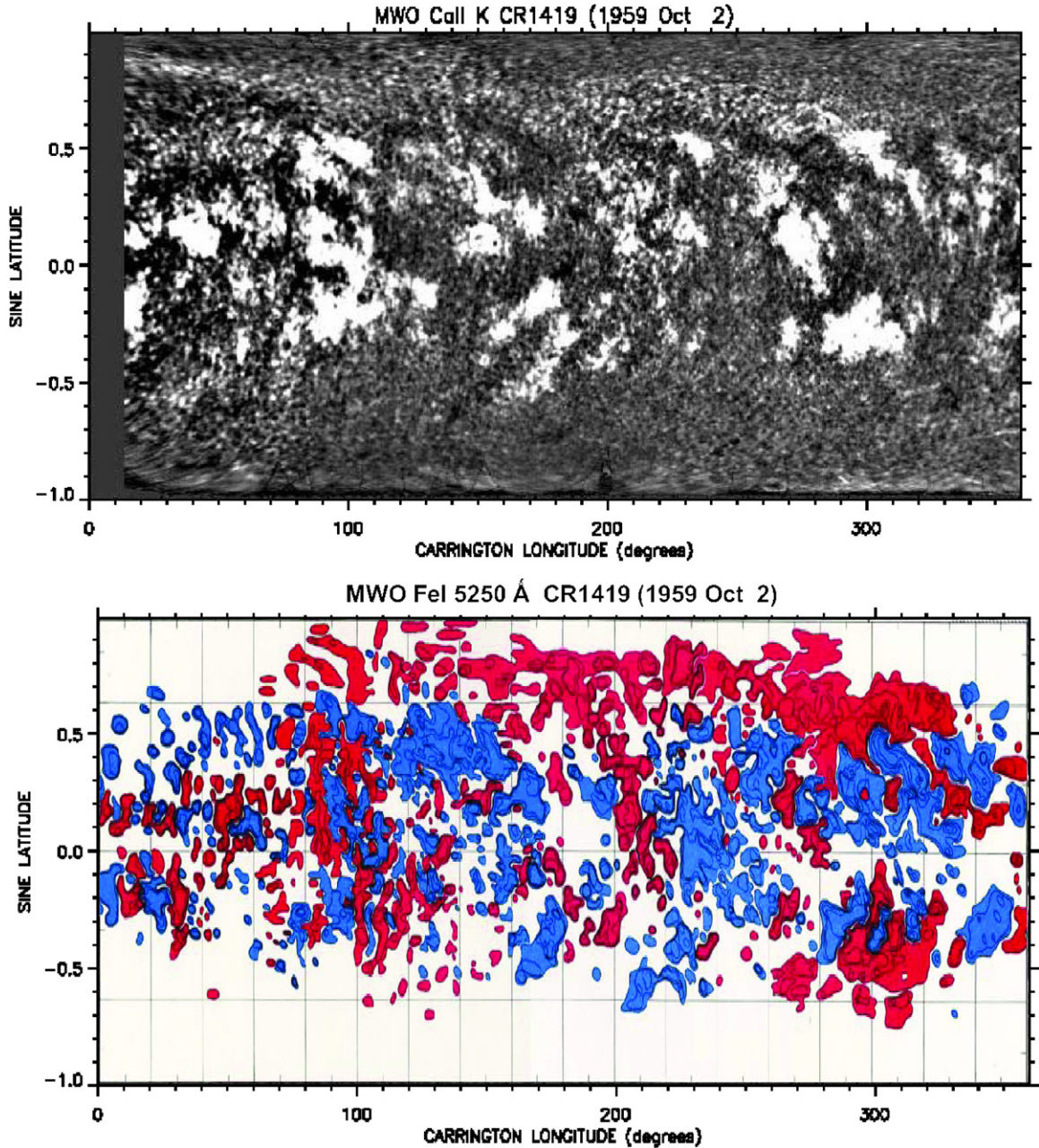


Figure 3. Carrington maps of K-line intensity (top) and MWO magnetic field (bottom) for rotation 1419. By this time, the large surge of trailing-polarity flux stretched across the entire northern hemisphere (but was cut off by data gaps at the left ends of the maps). In the magnetogram, blue refers to positive polarity and red refers to negative polarity.

In the south, the polar field reversed gradually during 1957 and became strong by the end of the year. In the north, the polar field remained weak until late in 1958 when it suddenly reversed. Figures 2 and 3 showed a large surge of trailing-polarity flux heading toward the north pole in 1959. Now, Figure 6 shows a large region of enhanced K-line emission heading poleward from the southern-hemisphere sunspot belt two years earlier in Carrington rotation 1394 (starting date 1957 November 19). We suppose that this was a surge of trailing-polarity (positive) flux on its way to strengthen the south polar field. This map also shows dark filaments winding between the numerous, closely spaced active regions, including one active region located at a north latitude $\sim 45^\circ$ (sine latitude ≈ 0.7). We have the impression that such high-latitude active regions occurred more frequently

in sunspot cycle 19 than in any other cycle during the years 1915–1985.

Figure 7 shows Carrington maps for rotation 1259 (starting date 1947 October 21) and 1261 (starting date 1947 December 14) when a large surge of chromospheric emission was headed toward the south pole. By 1947 December, that surge stretches across the entire southern hemisphere and is separated from the south pole by fragments of a polar crown filament. The presence of this filament implies that the south polar field had not yet reversed and that the surge had the negative polarity of the trailing fields of the southern hemisphere.

In Figure 8, the Carrington map for rotation 1245 (starting date 1946 October 4) shows a long disk filament winding between poleward migrating patterns of emission in the northern

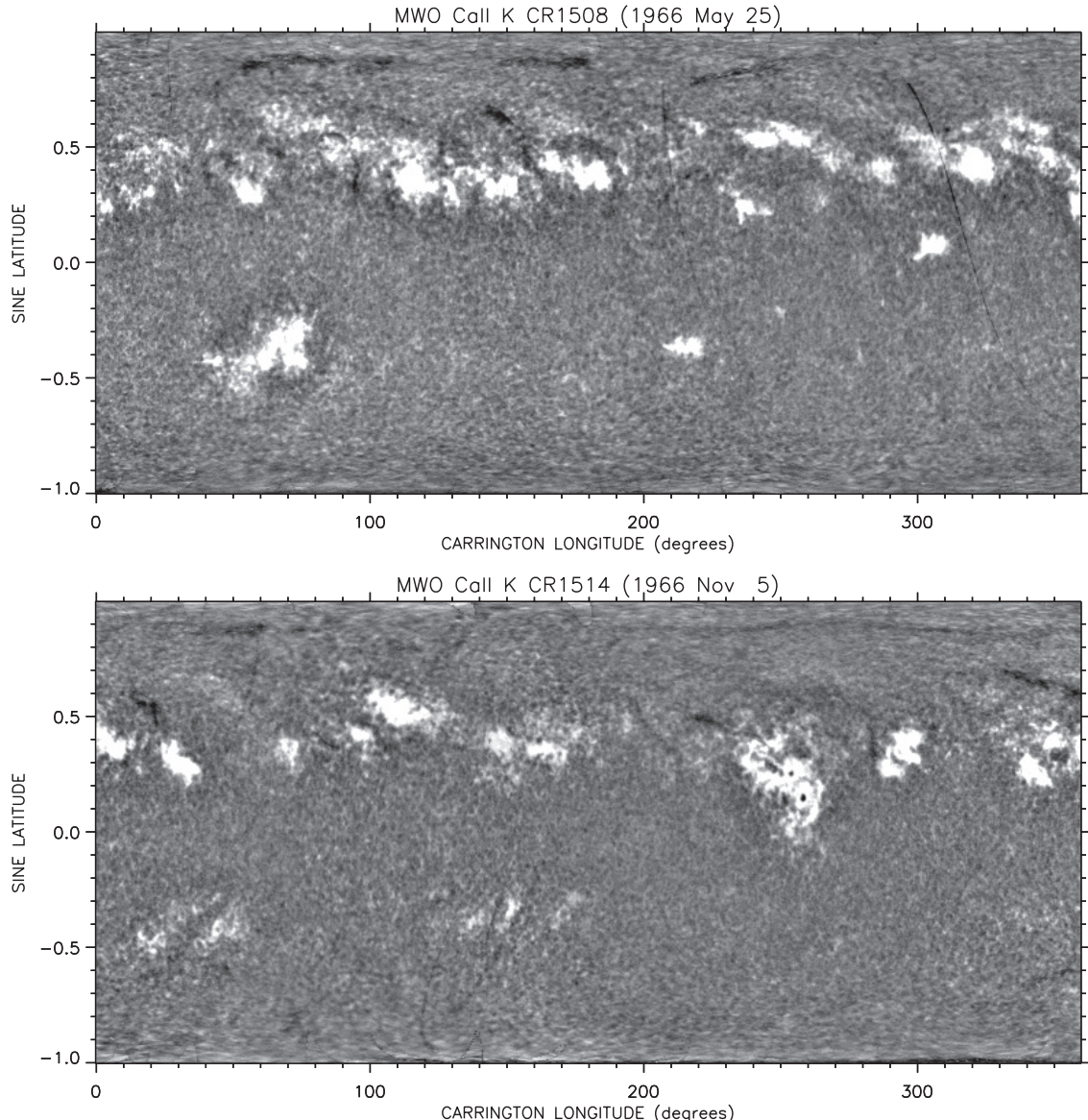


Figure 4. Carrington maps of K-line intensity for rotations 1508 (top) and 1514 (bottom), illustrating the strong north–south asymmetry of enhanced K-line emission during 1966.

hemisphere. This implies that both polarities were migrating poleward and that the filament was separating positive-polarity flux from the negative-polarity flux of the unreversed north polar field. In particular, the break in the filament near 200° longitude is similar to the polar-crown filament gaps that McIntosh (1980) identified in H α synoptic maps during sunspot cycles 20 and 21, and which contained extensions of the polar coronal holes. Thus, we suppose that this filament gap in 1946 October also contained an extension of the north polar coronal hole. This suggests the possibility of comparing these maps with long-term records of geomagnetic activity as a way of studying the origin and long-term evolution of the solar wind.

Figure 9 shows Carrington maps for rotation 1125 (starting date 1937 October 18) near the maximum of sunspot cycle 17 and rotation 1143 (starting date 1939 February 21) near the start of the declining phase of the cycle. By 1939, regions of enhanced calcium emission slant poleward and eastward with disk filaments along their boundaries.

Figure 10 shows Carrington maps for rotations 973 (starting date 1926 June 12) and 977 (starting date 1926 September 29)

during the rising phase of sunspot cycle 16. This was the weakest cycle during the interval 1915–1985. In rotation 977, several new active regions and their principal sunspots are visible in the northern hemisphere. A wide equatorial swath, devoid of strong activity, separates this northern-hemisphere activity belt from the broader distribution of decaying active regions in the southern hemisphere. The reduced visibility of disk filaments suggests that a wider spectral bandpass was used during this time.

Figure 11 shows the distribution of Ca II K-line emission during rotations 854 (starting date 1917 July 23) and 856 (1917 September 16) near the peak of the slightly stronger sunspot cycle 15. Even these images show some disk filaments and some faint patches of K-line intensity extending eastward and poleward from the activity belts.

Up to this point we have concentrated on the years around sunspot maximum, comparing the enhanced activity from cycle to cycle. Now, in contrast, we show Carrington maps obtained during sunspot minimum in 1954 when the polar regions contained relatively large numbers of faculae (Sheeley 2008)

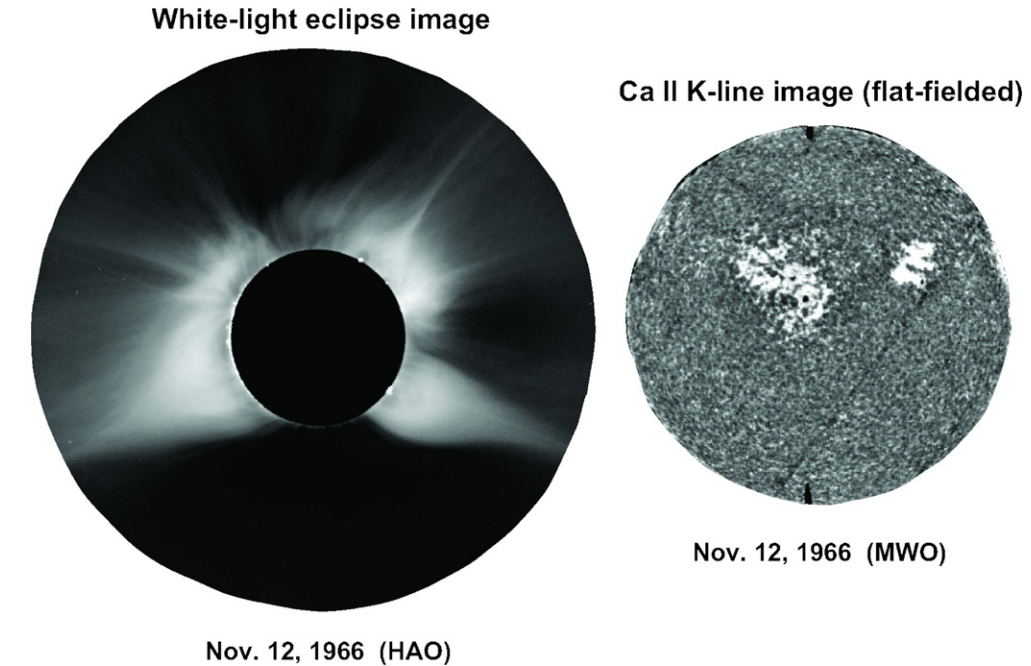


Figure 5. HAO eclipse photograph (left) and MWO flat-fielded Ca II K-line image (right). Although the sunspot cycle had advanced well into its rising phase in the northern hemisphere, the corona still showed its sunspot minimum appearance in the southern hemisphere.

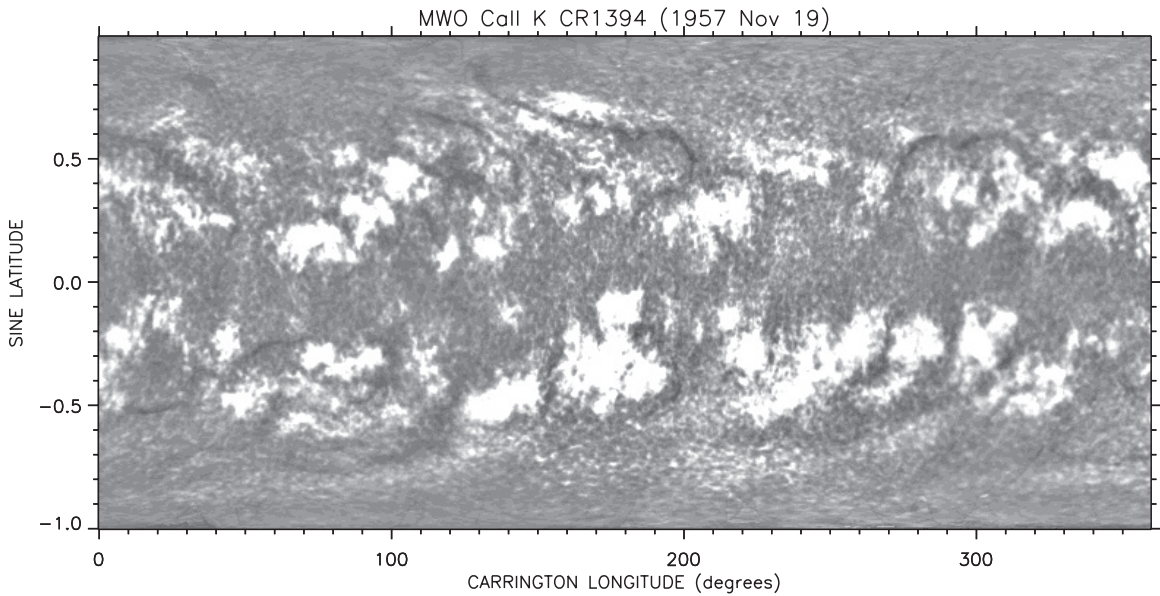


Figure 6. Carrington map of K-line intensity for rotation 1394. In 1957, the Sun was becoming increasingly crowded with active regions even at high latitudes, and a large wave of K-line emission was visible, migrating poleward from active regions in the southern hemisphere.

and the lower latitudes were relatively quiet. Figure 12 shows Carrington maps for rotations 1346 (starting date 1954 April 20) and 1351 (starting date 1954 September 3) when the south and north poles were tilted toward Earth. In the favorable hemisphere (south in spring, north in fall), the short, east–west elongated streaks correspond to polar faculae that have been stretched in the map construction.

In the unfavorable hemisphere, the brighter enhancements along the edges of the maps were produced by the distortion of high-latitude faculae near the edge of the disk and the blurring of these distorted regions in the map construction. Part of the adjacent darkened area corresponds to places that were invisible on the back side of the Sun as seen from Earth. However, an extra

part of this darkened area is caused by an artificial reduction of intensity for pixels that lie near the edge of the disk where a bidirectional interpolation was not possible. This extra area is lost when the scaling of the Carrington map exceeds this reduced intensity.

4. INITIAL STUDIES

As a first step in our analysis of these Carrington maps, we have constructed “butterfly diagrams” of longitudinally averaged intensity expressed as a function of time (horizontal axis) and sine latitude (vertical axis). The objective of this procedure was to see how the latitudinal distribution of enhanced

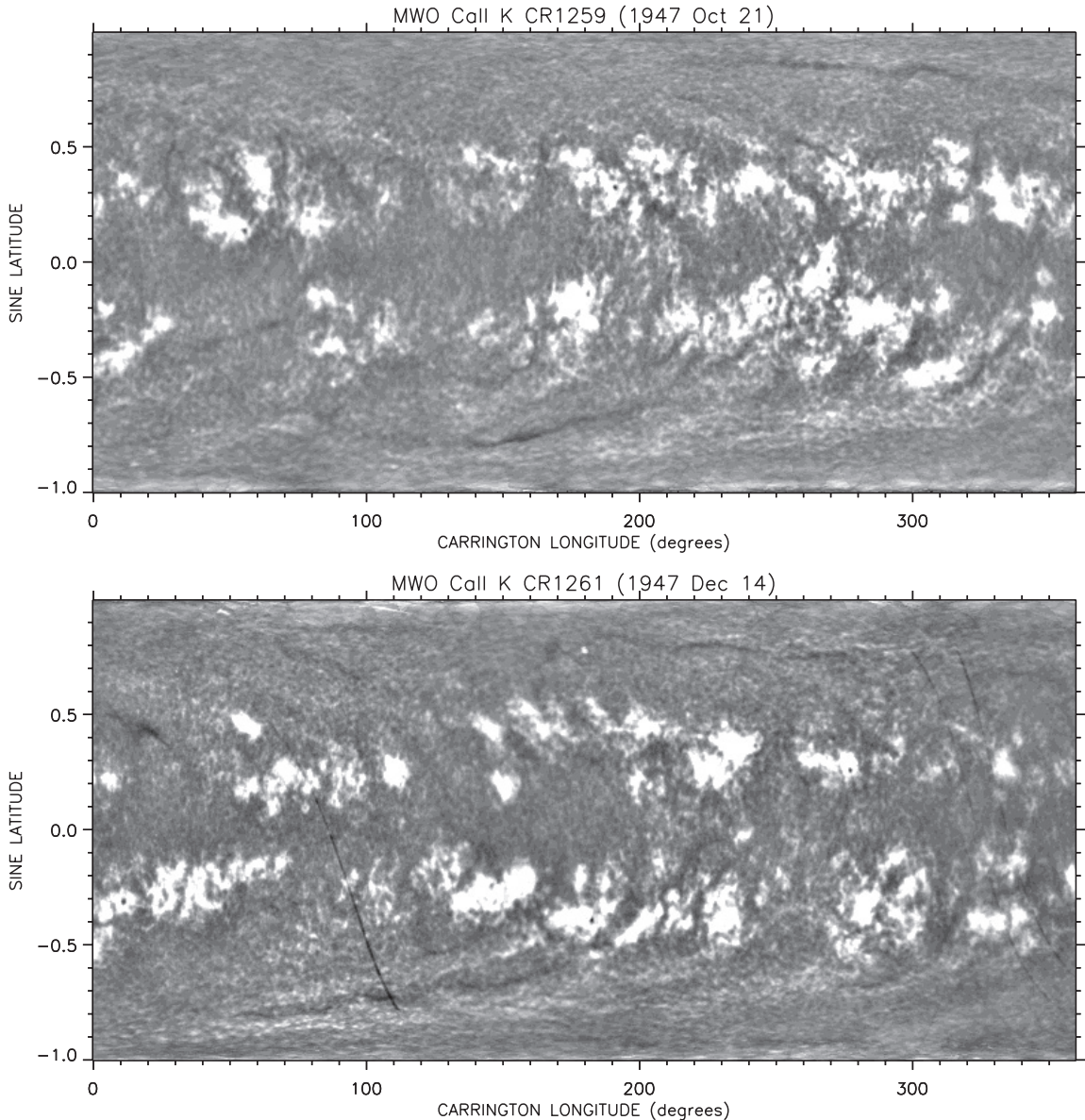


Figure 7. Carrington maps of K-line intensity for rotations 1259 (top) and 1261 (bottom) near the peak of sunspot cycle 18. A large wave of emission is visible migrating poleward and eastward from the southern-hemisphere sunspot belt. This stream is separated from the pole and from lower latitude regions by disk filaments.

calcium emission varies from cycle to cycle and, in particular, to see if we could detect the migration of flux from the sunspot belts to the poles.

The top panel of Figure 13 shows such a butterfly diagram for the entire interval 1915–1985. In this display, the butterfly wings of each sunspot cycle are not smooth, but have a fine structure composed of contributions from individual active regions. Some of these features slant steeply upward toward the poles, as seen in the northern hemisphere in 1951 and 1937 and in the southern hemisphere in 1947. Allowing for a transformation from sine latitude to latitude, their slopes lie in the range $10\text{--}20 \text{ m s}^{-1}$ and are comparable to the speeds of episodic poleward surges observed in longitudinally averaged maps of photospheric magnetic field (Howard & Labonte 1981; Wang et al. 2009). Thus, we suppose that these features are stalks of poleward surges that are not bright enough to be seen all the way to the poles.

We attempted to “normalize” the calcium intensities by dividing each Carrington map by its background intensity, taken

to be the most frequently occurring value in its histogram (i.e., the mode). Despite this attempt, the enhancement of intensity appears much greater in cycle 19 (which peaked in 1958) than in the other sunspot cycles. Based on the appearance of individual Carrington maps and their histograms, we suspect that the excessive intensity during cycle 19 has an instrumental or observational origin.

However, we do not yet know what this origin is. Bertello et al. (2010) found an enhancement in the widths of the intensity histograms of individual images during cycle 19 and Tlatov et al. (2009) found a similar enhancement of the plage contrast during that time, also using calcium images from the Mount Wilson archives. However, Tlatov et al. (2009) did not find a cycle-to-cycle variation in their measurements of calcium images obtained at the Kodaikanal Observatory, and speculated that the enhancements recorded on the Mount Wilson images were caused by a systematically narrower bandpass during cycle 19.

The less frequent appearance of disk filaments in our Carrington maps during cycles 15–17 suggests that the bandpass

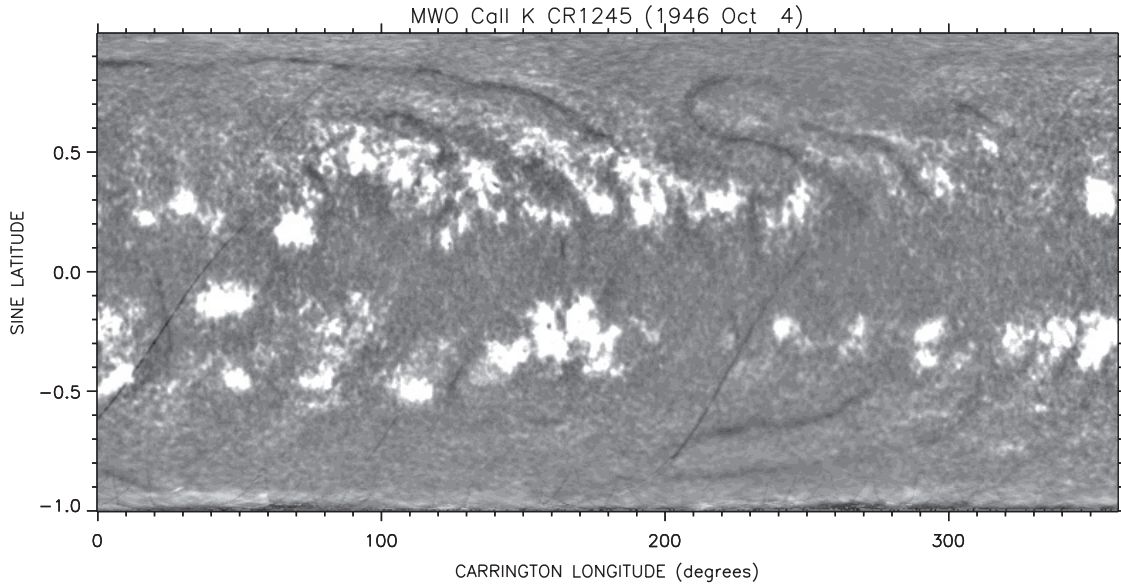


Figure 8. Carrington map of K-line intensity for rotation 1245, showing numerous disk filaments, including one winding between patterns of migrating flux in the northern hemisphere.

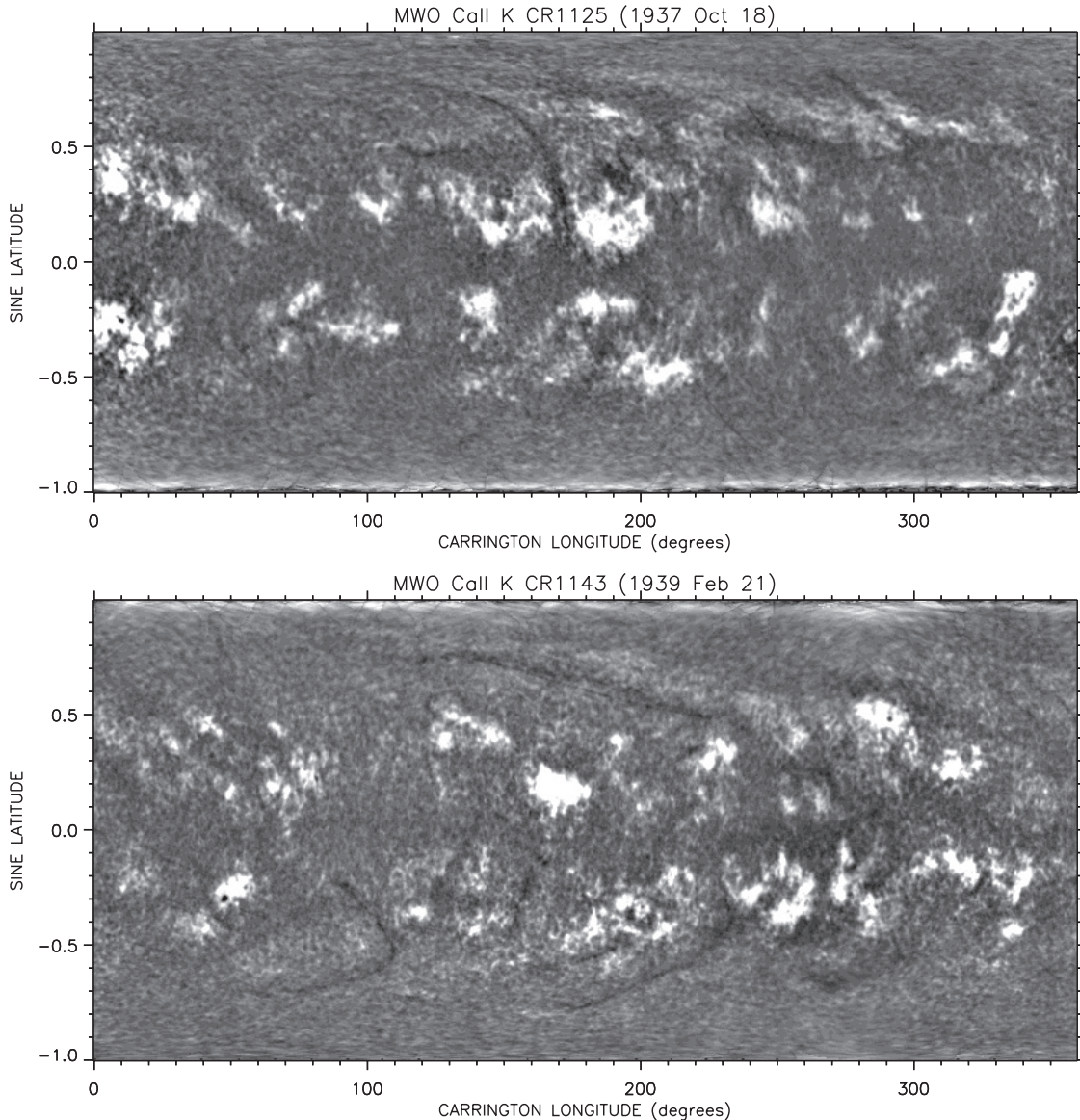


Figure 9. Carrington map of K-line intensity for rotations 1125 and 1143, showing the conditions near sunspot maximum and the initial declining phase of cycle 17.

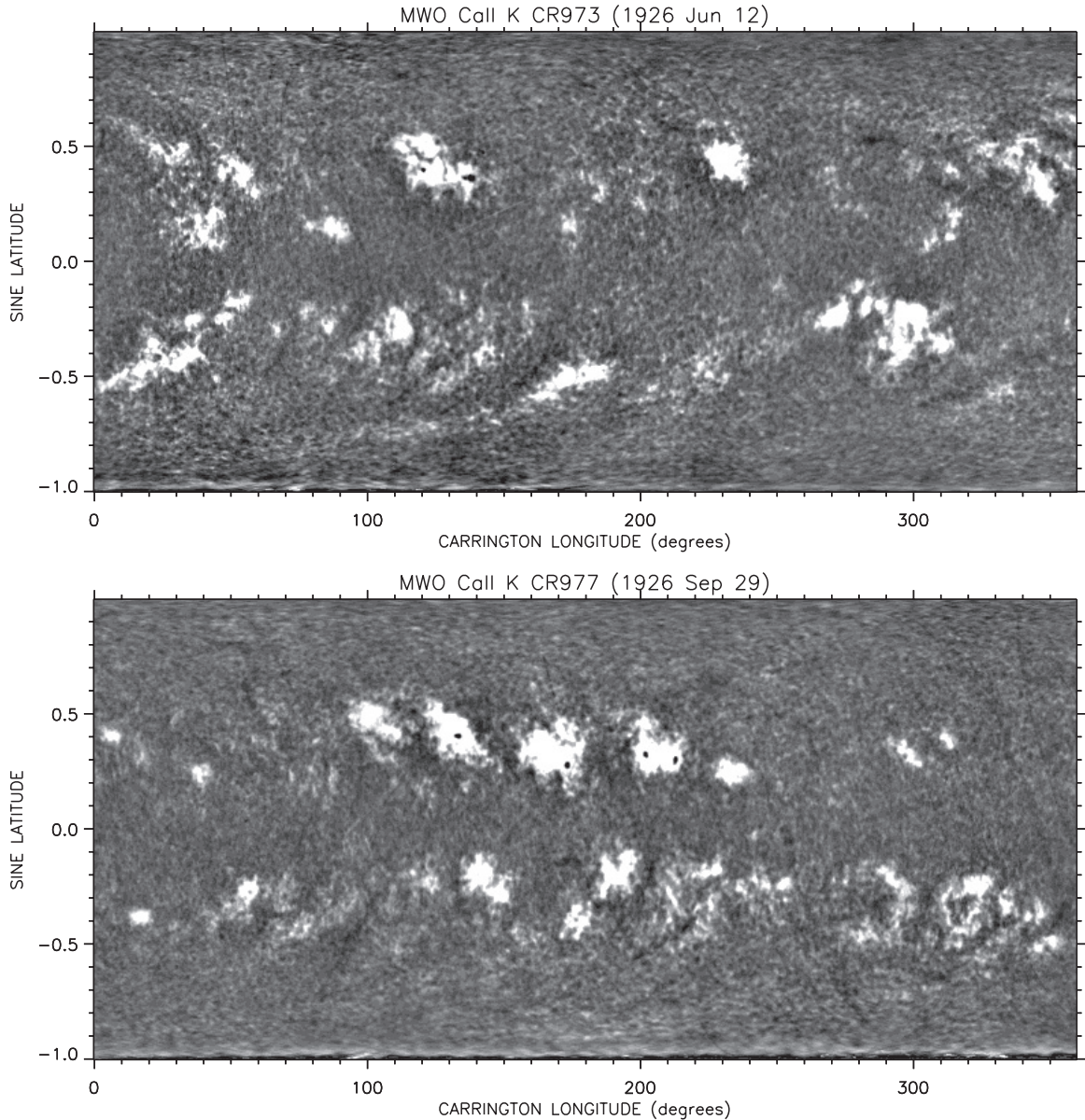


Figure 10. Carrington maps of K-line intensity for rotations 973 (top) and 977 (bottom) during the rising phase of sunspot cycle 16.

must have been wider during the early years at Mount Wilson than during the later years (cycles 18–21). This is also consistent with the increased visibility of sunspots during those years, as pointed out by Ermolli et al. (2009) and Foukal et al. (2009). However, the visibility of filaments does not seem to be systematically greater during cycle 19 than during cycles 18 or 20 (or even 21). Consequently, we wonder if other instrumental or observational effects may contribute to the unique intensity profiles during cycle 19. It is plausible that contributions might come from the quality of the grating, the amount of scattered light in the spectrograph, and the characteristics of the photographic emulsion and processing, as well as a narrow spectral bandpass.

The top panel of Figure 13 contains scalloped regions along its upper and lower edges. The temporal locations of these dark indentations (autumn at the southern edge and spring at the northern edge) are consistent with the B_0 effect, caused by the 7.25° tilt of the Sun's rotation axis relative to the ecliptic. However, the amplitude of the observed variation is neither

constant with time nor symmetric between the two hemispheres. In principal, the 7.25° annular change in B_0 corresponds to a 1% variation of sine latitude if the contributions come from regions near the central meridian, and to a 3% variation if the contributions come from 60° away from the central meridian. The irregular cadence of “good” images would then produce temporal variations of amplitude, as observed. However, the effect is enhanced by an intensity reduction at the poorly observed polar limb and our inability to perform a bidirectional interpolation there. This causes the amplitude of the dark scalloping to increase with the contrast that is applied to the display.

Although we have not yet found a way to avoid this effect, we can reduce it by shifting the top panel by one year and then subtracting it from the original, unshifted panel. The middle panel of Figure 13 shows the resulting map (shifted leftward by 0.5 yr to center the difference signals on the original, unshifted features). The bottom panel shows the corresponding map when the vertical streaks are convoluted away before shifting and

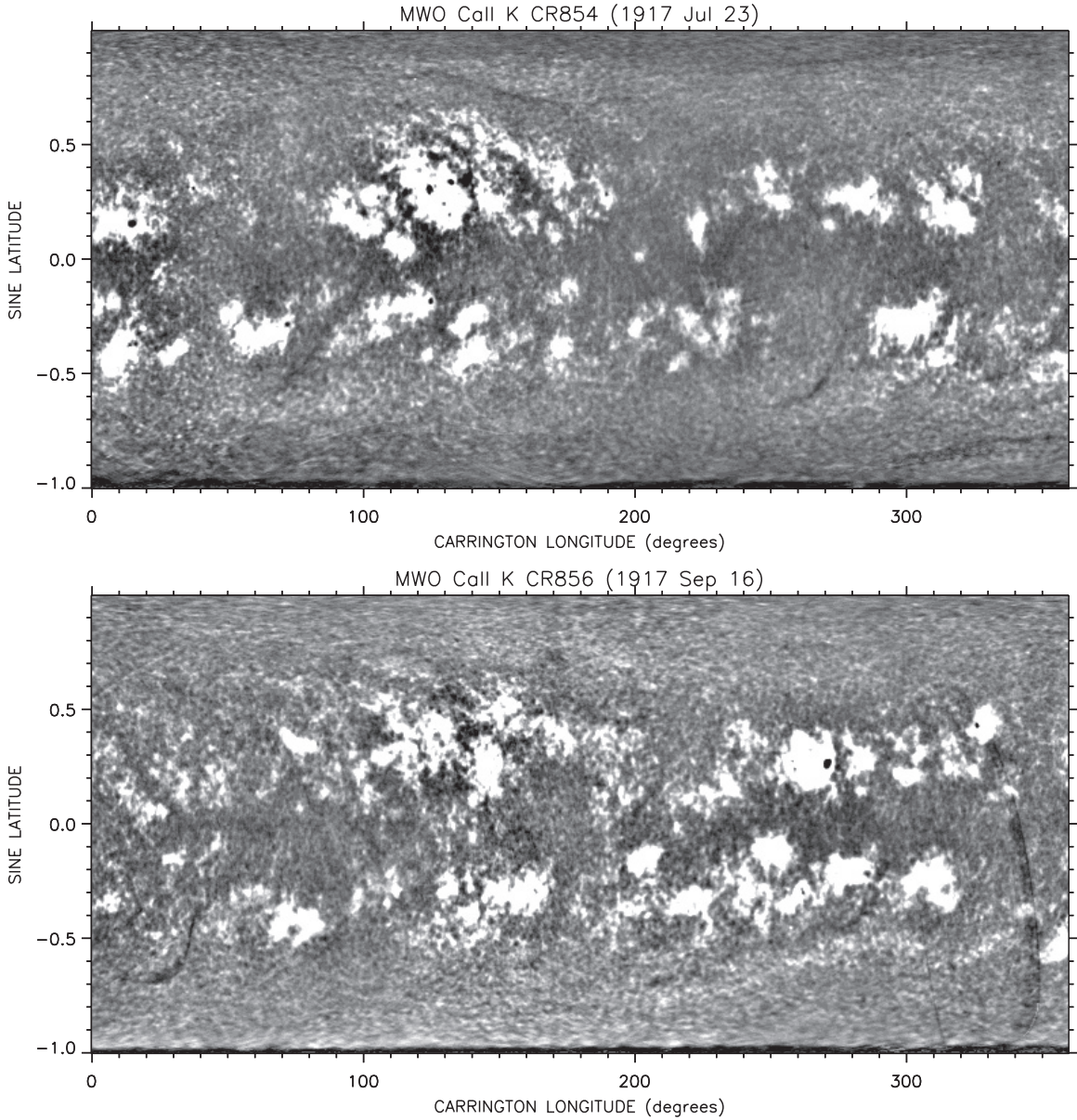


Figure 11. Carrington maps of K-line intensity for rotations 854 (top) and 856 (bottom) near the maximum of sunspot cycle 15.

subtracting. Each of these panels shows a series of short tracks at high latitudes in each hemisphere, apparently indicating the poleward migration of prominences and the magnetic neutral lines that accompany them. Converting from sine latitude to latitude, we find that the slopes of these tracks correspond to speeds in the range $\sim 2\text{--}4 \text{ m s}^{-1}$. Thus, the magnetic neutral lines of the large-scale field move poleward at speeds that are much slower than the $\sim 10\text{--}20 \text{ m s}^{-1}$ surges of flux that drive them.

In the middle and bottom panels of Figure 13, we can see prominence migrations in the northern hemisphere during the rising phase of sunspot cycles 17–21 and in the southern hemisphere during the rising phase of cycles 18–21. In addition, multiple reversals seem to have occurred at both poles during cycle 19 and at the south pole in cycle 21. In these difference images, most of the tracks are two-toned with leading-white/trailing-black signatures, as expected for dark disk filaments. However, during cycle 19, some of these tracks had reversed (leading-black/trailing-white) signatures corresponding to bright features

on the unsubtracted image. Thus, the enhanced visibility during cycle 19 seems to be revealing the poleward migration of bright regions of calcium emission as well as the dark disk filaments that accompany them.

The top panel of Figure 14 shows the butterfly diagram when the longitudinal average spans the 25 brightest pixels at each latitude. Our objective is to show the latitude distribution of enhanced calcium emission. Regardless of how the intensity is calibrated, there can be no doubt that cycle 19 contained a much wider latitudinal distribution of emission than any other cycle in this 70 year interval. High-latitude extensions indicate active regions as far poleward as $50^\circ\text{--}55^\circ$ (sine latitude approximately 0.8), and some fainter emission is visible all the way to the poles.

A filtered version of this display is shown in the middle panel. Here, the extra width of cycle 19 is clearly visible, especially compared to the relatively weak cycles 16 and 20. In cycle 19, the activity at high latitude is partially masked by the annual variations, but these annual variations can be reduced by a one year shift and subtraction, as shown in the bottom panel.

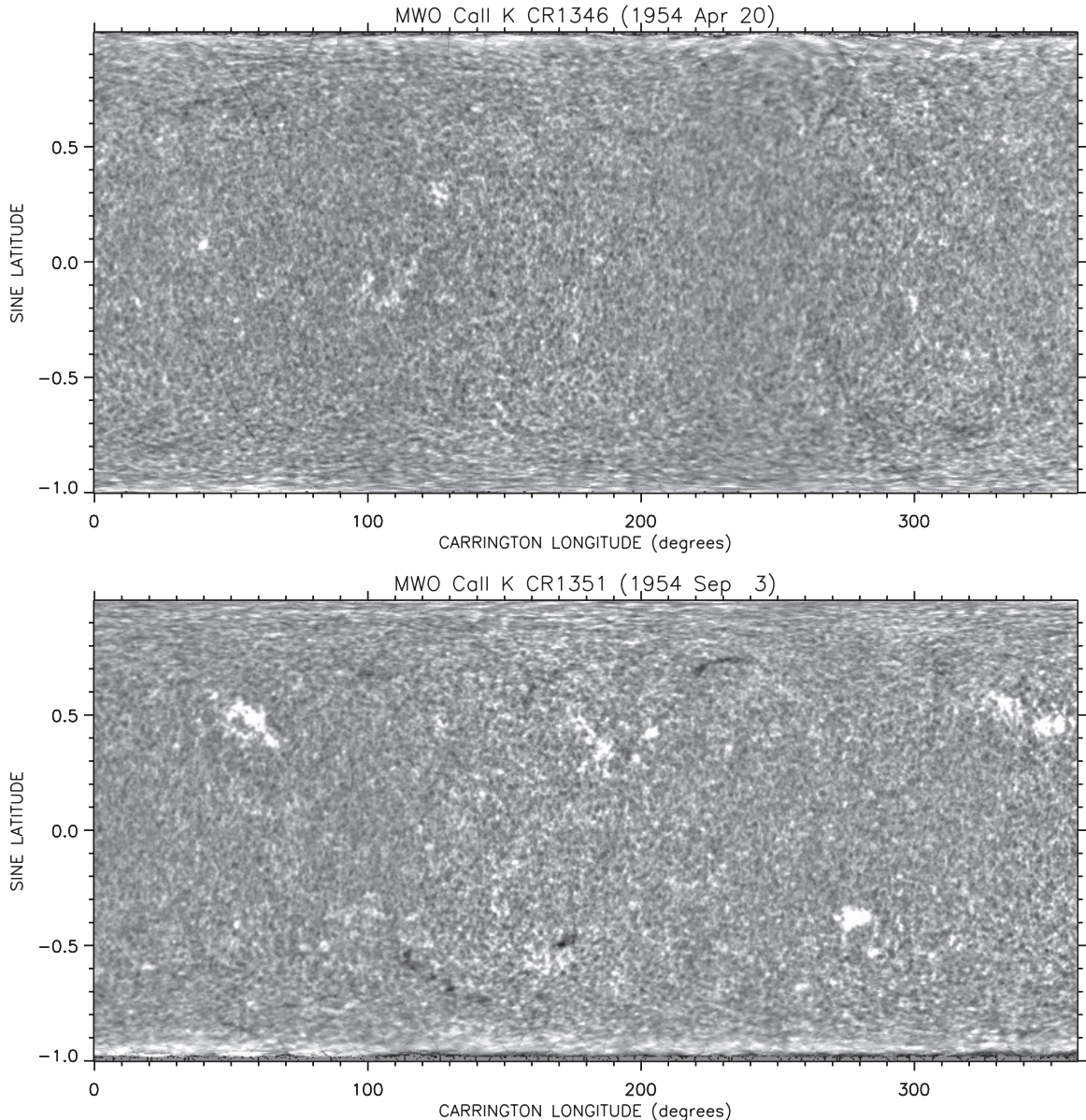


Figure 12. Carrington maps of K-line intensity for rotations 1346 (top) and 1351 (bottom), showing spring and fall views of the Sun during the 1954 sunspot minimum. At high latitudes in the favorable hemisphere (south in rotation 1346; north in rotation 1351), the short streaks in the east–west direction are caused by polar faculae, but in the unfavorable hemisphere, the enhanced areas along the edges of the maps are artifacts of the map construction.

Now, the enhanced activity in 1958 is visible all the way to the poles.

The middle and lower panels also emphasize the extended interval of quiet conditions that occurred in the southern hemisphere in the mid-1960s between cycle 19 and 20. As we have mentioned previously, this lack of activity is comparable to the unusually quiet conditions that occurred in both hemispheres during the recent sunspot minimum in 2008–2009 and during the minimum that occurred in 1913, just prior to the start of the Carrington maps described in this paper (Sheeley 2010).

The poor representation of poleward surges in these longitudinally averaged displays is not surprising. Poleward surges were neither visible in butterfly diagrams of photospheric faculae, derived from continuum images obtained with the Michelson Doppler Imager (MDI) on the *Solar and Heliospheric Observatory* during 1996–2005 (Sheeley & Warren 2006), nor in longitudinally averaged maps of the absolute value of the MDI photospheric field. Evidently, the magnetic polar-

ity is essential for detecting the surges when averaging over longitude.

The so-called super-synoptic construction technique (Ulrich et al. 2002) is a convenient way of combining these maps without averaging them in longitude. The technique is very simple. We just squash the Carrington maps in longitude, reverse their east–west directions so that time runs continuously from left to right, and place the reversed minimaps in chronological order. It is the same technique that we have used previously to make height/time maps (so-called jmaps) to track coronal ejections outward from the Sun (Sheeley et al. 1999). In this paper, we compress the longitudinal scale by a factor of nine, reducing the horizontal dimension of each Carrington map from 720 pixels to 80 pixels, and we display the resulting stackplots of these compressed maps in 1.8 yr segments.

The panels in Figure 15 span most of sunspot cycle 19. During the rising phase of the cycle (top panel), the growing belts of K-line emission are clearly visible. In addition, horizontal chains

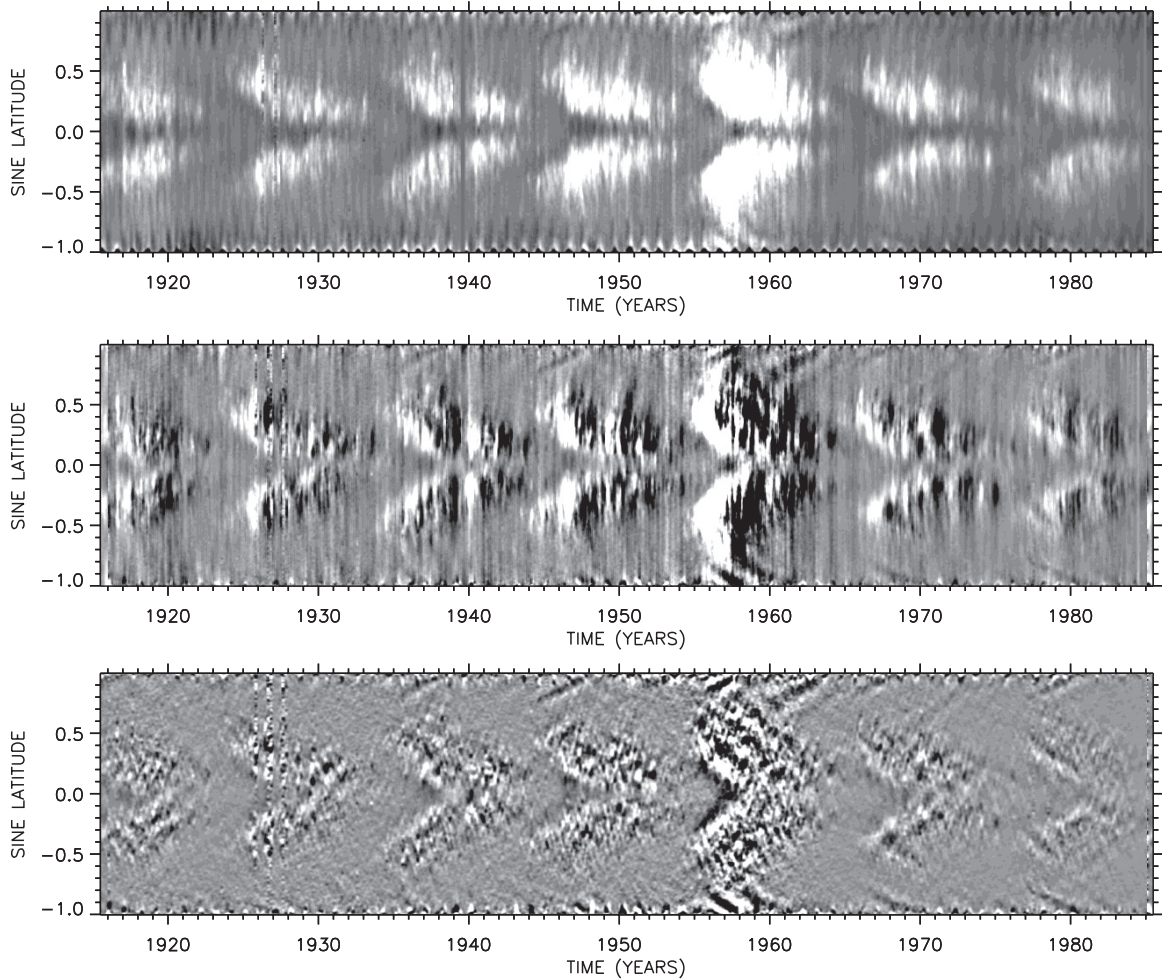


Figure 13. Displays of the longitudinally averaged K-line intensity (top), the one year shifted difference of this map from itself (middle), and the one year shifted difference after the original map has been filtered to remove vertical streaks (bottom). The subtractions remove annual variations and reveal the $2\text{--}4 \text{ m s}^{-1}$ poleward migrations of disk filaments and their magnetic neutral lines as two-toned tracks slanting toward the poles.

of two-toned features are faintly visible near the north and south poles during 1956–1957, with the white portion closer to the pole than the black portion. These structures correspond to dark polar crown filaments surrounding enhanced K-line emission in the polar regions. These features gradually contract toward the poles and disappear during 1956–1957, indicating the weakening and disappearance of the polar fields.

During 1957–1959 (second panel), a sequence of curved features projects out of the southern-hemisphere activity belt and extends toward the south pole. Although these features begin as entirely white regions of enhanced K-line emission, they gradually develop dark areas along their equatorward sides. Individual Carrington maps indicate that these dark areas are disk filaments, which presumably separate the migrating flux from lower latitude regions of opposite polarity. A similar surge appears in the northern hemisphere during 1959–1960 (third panel) and again during 1960–1961 (bottom panel). Like the southern-hemisphere surge during 1957–1959, both of these northern-hemisphere surges are two-toned, with dark prominence material along the equatorward sides of the migrating regions of enhanced K-line emission.

The southern-hemisphere surge bent horizontally to form an axisymmetric part of the high-latitude field above 60° latitude in 1959 when large numbers of south polar faculae became visible (Sheeley 2008). The first northern-hemisphere surge reached

60° latitude in 1960 and the second surge arrived there in 1961 to maintain the structure for three years, when large numbers of north polar faculae were visible. A longstanding puzzle is why the numbers of polar faculae decreased suddenly at the south pole in 1960 and at the north pole in 1962. Perhaps further study will reveal that these surges were bipolar, with leading polarity following trailing polarity to the poles.

Figure 16 shows the evolution in 1966–1967 during the rising phase of cycle 20. This time, we see the increased activity, first in the north and then in the south. Poleward of the northern-hemisphere activity, two-toned structures are faintly visible migrating toward the north pole during 1966–1967, with the brighter side toward the pole. This polar crown prominence seems to disappear around 1967.5, corresponding to the disappearance of the north polar field. The formation of the south polar crown is just beginning at that time, as strong magnetic activity begins in the southern hemisphere. This observation supports previous studies which suggest that the formation and migration of the polar crown prominences accompany the onset of new-cycle activity (Ananthakrishnan 1952; Babcock 1961; Leighton 1964; Makarov & Sivaraman 1989).

Figure 17 shows the evolution during sunspot cycle 18. Segments of polar crown filaments are faintly visible in the north in 1946 during the rising phase of the cycle (top panel),

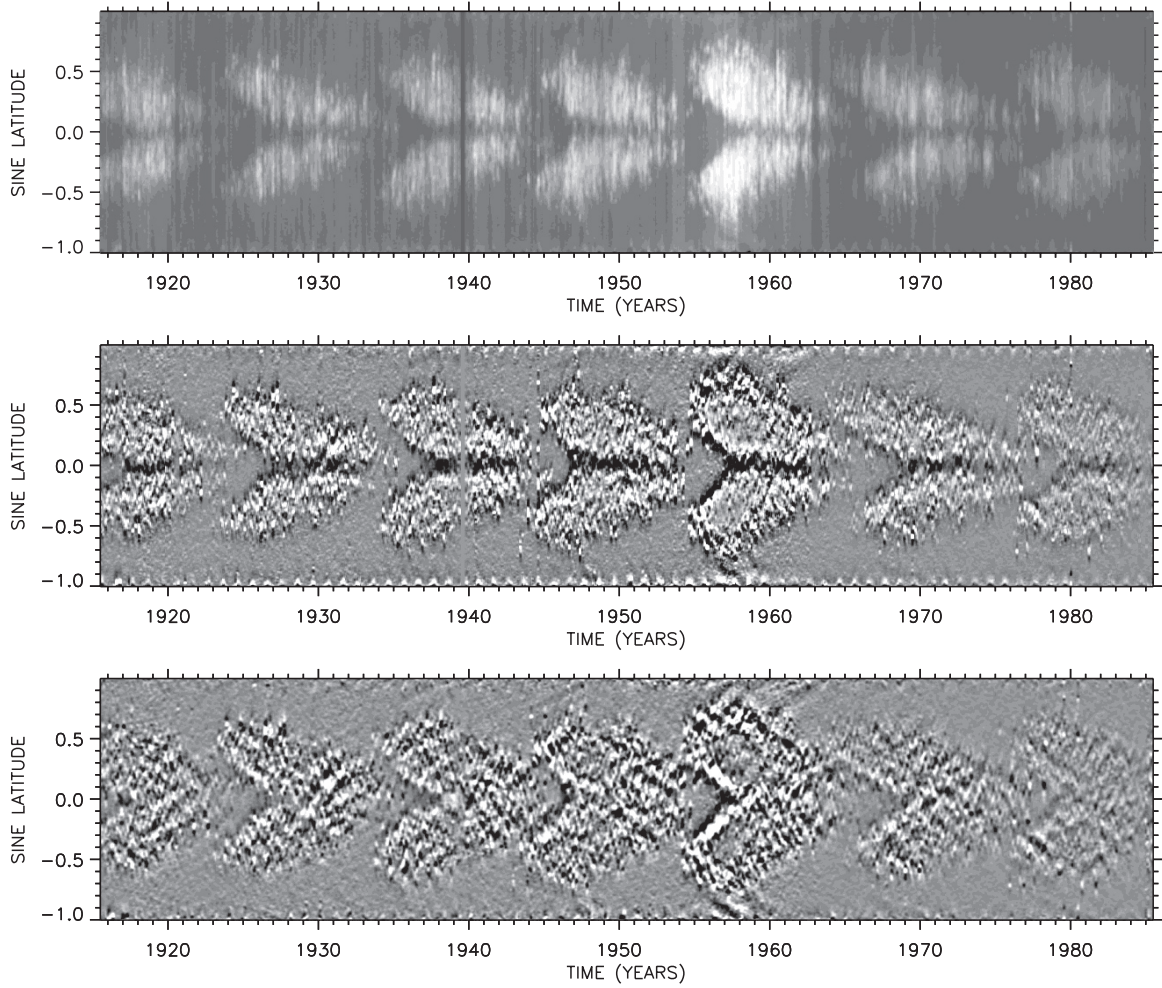


Figure 14. Average intensity of the 25 brightest pixels in each map (top), a filtered version of this map (middle), and a one year shifted difference of the filtered map from itself (bottom), showing the latitude distribution of calcium emission during the years 1915–1985. In cycle 19, the distribution is especially broad, with tracks occasionally extending to the poles.

but filaments are not visible in the south. We have already seen some of these filaments in Figure 8. During 1947–1948 (second panel), a large poleward surge is visible in the southern hemisphere and another is faintly visible across the equator from it in the northern hemisphere. The southern-hemisphere surge corresponds to the poleward stream that we identified in the maps of CR1259 and CR1261 in Figure 7. That stream had a polar crown filament along its poleward edge, indicating that the south polar field had not yet reversed.

Thus, unlike the cycle 19 surges, which seemed to be strengthening the new polar fields by adding more flux of the same polarity, this cycle 18 surge may have been weakening the old south polar field by adding flux of opposite polarity. Perhaps this is why these two surges during 1947–1948 died soon after reaching the pole and did not retain long-lived axisymmetric signatures like those that occurred in cycle 19. Even fainter surges are visible in the northern hemisphere in 1949–1950 and again in 1951–1952 (bottom panel). These faint surges correspond to the steep stalks of emission that we found in the map of longitudinally averaged intensity (Figure 13).

5. SUMMARY AND DISCUSSION

In this paper, we have described our procedure for making Carrington maps of Ca II K-line intensity for the years

1915–1985 and we have provided a sample of those maps with our interpretations. In addition, we have attempted to summarize these maps in longitudinally averaged “butterfly” diagrams and in super-synoptic displays. The excessive brightness variations obtained during cycle 19 are consistent with the increased widths of the histograms measured by Bertello et al. (2010) and with the enhanced plage contrast measured by Tlatov et al. (2009) for the individual images in the Mount Wilson archive. Like those authors, we suppose that these brightness variations reflect unique characteristics of the instrument or observing procedure during this time, rather than special properties of the Sun.

On the other hand, a greater part of the butterfly diagram was covered by enhanced calcium emission during cycle 19 than during any other sunspot cycle. In fact, the increased activity at high latitudes and the correspondingly wider belts of activity caused the butterfly wings to be broader during cycle 19 than during earlier and later cycles. The eruption of flux at high latitude may have been responsible for the greater visibility of poleward migrating regions of enhanced calcium emission during cycle 19 than during the other cycles.

By averaging out the B_0 variations, we were able to enhance the visibility of poleward migrating disk filaments during cycles 17–21, and therefore to infer the times of polar field reversal during those cycles. These filaments showed a $2\text{--}4 \text{ m s}^{-1}$

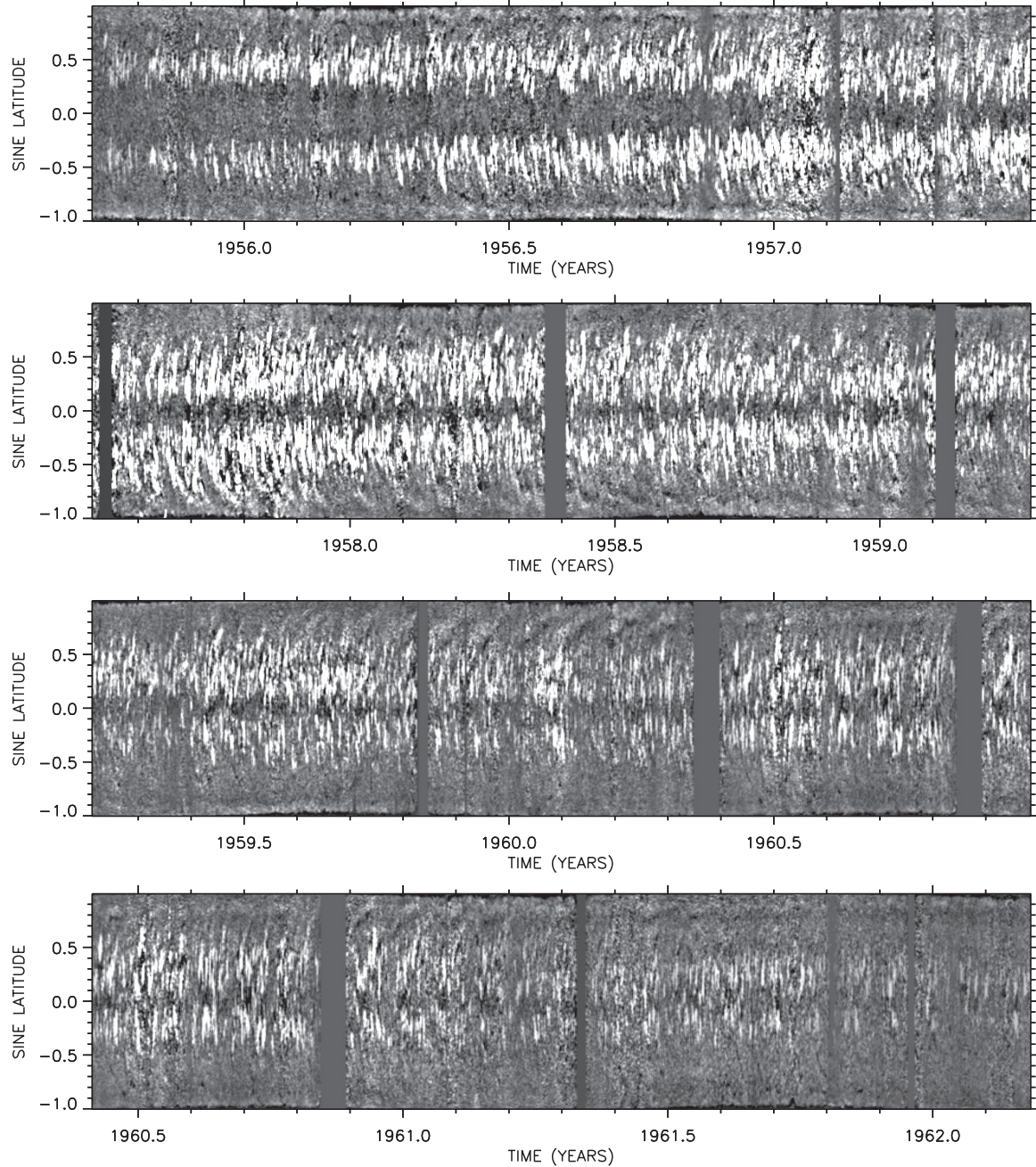


Figure 15. Latitude/time displays of K-line intensity during sunspot cycle 19. Disk filaments migrate slowly to the poles during 1956–1957 (top panel). As solar activity declines, major poleward surges of flux become visible, going to the south pole in 1957–1959 (second panel), and to the north pole in 1959–1960 (third panel) and 1960–1961 (bottom panel).

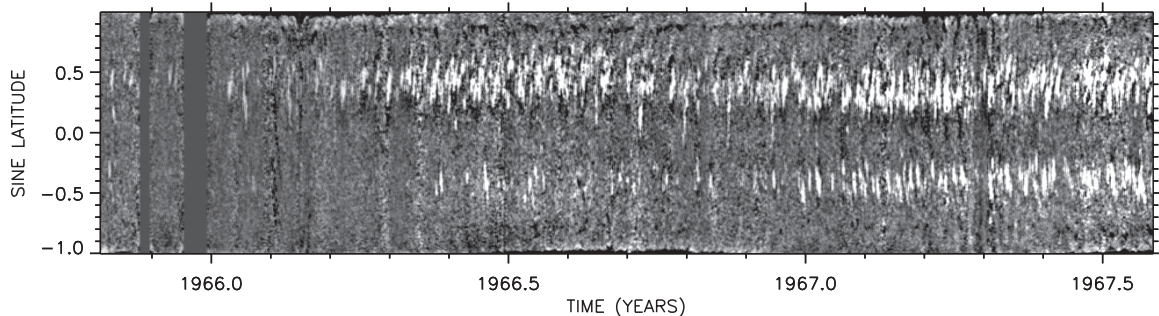


Figure 16. Latitude/time display of K-line intensity during 1966–1967 when solar activity was well into its rising phase in the north, but only beginning in the south. A polar crown filament is faintly visible poleward of the northern-hemisphere activity, and can be seen migrating very slowly toward the north pole.

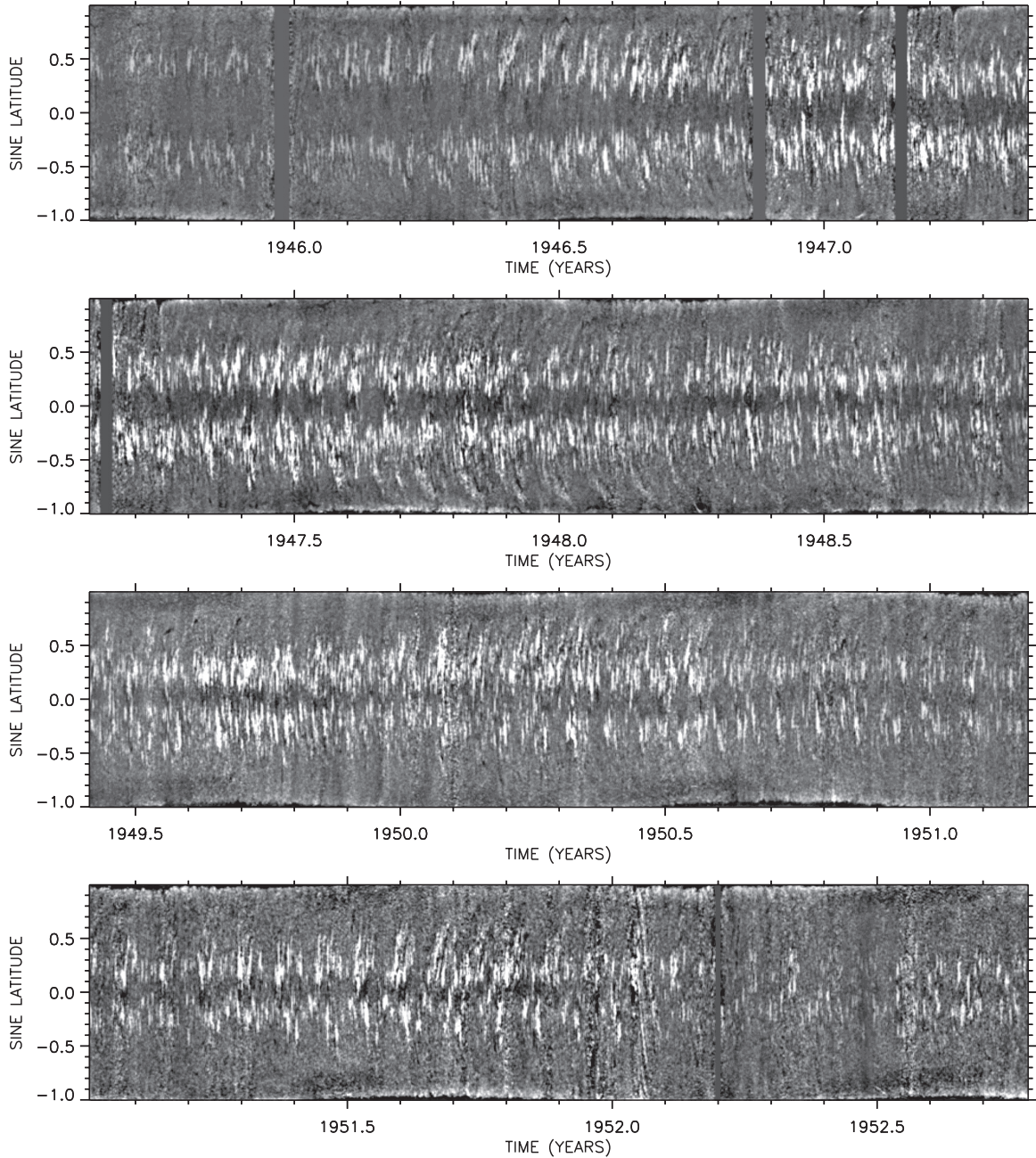


Figure 17. Latitude/time displays during cycle 18. Some polar crown prominences are faintly visible in 1946 (top panel). During 1947–1948 (second panel), a poleward surge is clearly visible in the south, and another is faintly visible in the north. Surges are also faintly visible in the north in mid-1950 (third panel), and again in mid-1951 (bottom panel).

poleward migration speed, which is significantly lower than the $10\text{--}20 \text{ m s}^{-1}$ speed with which flux typically moves poleward from its origin in the sunspot belts (Howard & Labonte 1981). This suggests that flux is carried to the poles in relatively small amounts which gradually chip away at the much larger fluxes of opposite polarity that accumulated there during the previous cycle.

A detailed examination of the middle and bottom panels of Figure 13 reveals multiple tracks going poleward in both hemispheres during cycle 19. From a study of H α synoptic charts, Makarov & Sivaraman (1989) inferred multiple reversals of the north polar field during cycle 19. However, those reversals occurred between 1958 and 1960, whereas the calcium tracks reached the north pole in 1957 and 1962–1963. Also, Makarov

& Sivaraman (1989) did not infer multiple reversals at the south polar field during cycle 19. Thus, we seem to be tracking different poleward migrations, at least during cycle 19. During cycles 20 and 21, the calcium tracks match the migrations of the neutral lines in longitudinally averaged displays of the photospheric magnetic field, but not the steeper tracks of the poleward surges of flux as shown in Figure 2 of Wang et al. (2009).

In general, the butterfly diagrams of enhanced calcium emission do not show the classic poleward surges of flux that are so prominent on longitudinally averaged maps of photospheric magnetic field. As discussed previously (Sheeley & Warren 2006), this may be partly due to the lack of a sign that distinguishes trailing polarity from leading polarity in the

calcium maps. However, the reduced visibility of the calcium surges may also be due to the relatively low sensitivity of the calcium emission to magnetic fields, especially for weak fields spreading away from their sources in the activity belts.

We were able to track some of these poleward surges during cycles 18 and 19 by using super-synoptic displays, which avoid the longitudinally averaging process of the conventional butterfly diagrams. In these displays, the surges shoot out relatively quickly from the sunspot belts at speeds on the order of $10\text{--}20 \text{ m s}^{-1}$, and eventually form symmetrized patterns that drift slowly to the poles at speeds of $2\text{--}4 \text{ m s}^{-1}$.

We are beginning to study these poleward motions by comparing the super-synoptic maps with the frames of a time-lapse movie spanning the entire interval 1915–1985. This movie provides a rapid way of examining the maps and revealing the origin and evolution of individual magnetic structures. We have already used it to select Carrington maps for this paper and expect it to be useful for comparing the magnetic activities of different sunspot cycles as we move farther into the data analysis phase of this research.

We are grateful to Roger Ulrich (UCLA) and Luca Bertello (NSO) for encouragement and for helping us to obtain the flat-fielded Mount Wilson Observatory Ca II K-line images. Roger made an appreciable effort to search the observing records for information about the widths of the spectroheliograph slits and he sent us a copy of Larry Webster's (UCLA) summary of the gratings that were used at the MWO spectroheliograph. We appreciate the time that he has taken to read this paper and to suggest ways of improving it.

We are also grateful to Jack Harvey (NSO) for helpful advice about the techniques for making Carrington maps, and to Alexis Rouillard (GMU) for contributing to numerous luncheon discussions of map making. Bob Howard (NSO emeritus) provided several helpful suggestions, including the idea of constructing super-synoptic maps. We also thank him for permission to use magnetograms from the Atlas of Mount Wilson Magnetograms, and we thank John Seely (NRL) for making seamless scans of those magnetograms. We would like to acknowledge Yi-Ming Wang (NRL) whose research on meridional flow provided some of the stimulus for this work, and Guillermo Stenborg (Interferometrics Inc.) who helped us to filter the butterfly diagrams. The digitization of the Mount Wilson Solar Photographic Archive has been supported by the National Science Foundation through Grant 0236682 to the University of California at Los Angeles. At NRL, financial support was provided by NASA and the Office of Naval Research.

REFERENCES

- Ananthakrishnan, R. 1952, *Nature*, **170**, 156
 Babcock, H. D. 1959, *ApJ*, **130**, 364
- Babcock, H. W. 1961, *ApJ*, **133**, 572
 Bailey, W. L., & Sheeley, N. R., Jr. 1969, *Sol. Phys.*, **7**, 2
 Baumann, I., Schmitt, D., Schüssler, M., & Solanki, S. K. 2004, *A&A*, **426**, 1075
 Bertello, L., Ulrich, R. K., & Boyden, J. E. 2010, *Sol. Phys.*, **264**, 31
 Bumba, V., & Howard, R. 1965, *ApJ*, **141**, 1502
 Charbonneau, P. 2005, *Living Rev. Sol. Phys.*, **2**, 2
 Choudhuri, A. R., Schüssler, M., & Dikpati, M. 1995, *A&A*, **303**, L29
 Cranmer, S. R., Hoeksema, J. T., & Kohl, J. L. (eds.) 2010, *ASP Conf. Ser.* 428, SOHO 23: Understanding a Peculiar Solar Minimum (San Francisco, CA: ASP)
 Dikpati, M. 2005, *Adv. Space Res.*, **35**, 322
 Dikpati, M., & Gilman, P. A. 2009, *Space Sci. Rev.*, **144**, 67
 Ellerman, F. 1919, *PASP*, **31**, 16
 Ermolli, I., Solanki, S. K., Tlatov, A. G., Krivova, N. A., Ulrich, R. K., & Singh, J. 2009, *ApJ*, **698**, 1000
 Foukal, P., Bertello, L., Livingston, W. C., Pevtsov, A. A., Singh, J., Tlatov, A. G., & Ulrich, R. K. 2009, *Sol. Phys.*, **255**, 229
 Foukal, P., & Lean, J. 1988, *ApJ*, **328**, 347
 Harvey, J., & Worden, J. 1998, in *ASP Conf. Ser.* 140, Synoptic Solar Physics, ed. K. S. Balasubramaniam, J. Harvey, & D. Rabin (San Francisco, CA: ASP), **155**
 Howard, R., Bumba, V., & Smith, S. F. (eds.) 1967, *Atlas of Solar Magnetic Fields* (Washington, DC: Carnegie Institution)
 Howard, R., & Labonte, B. J. 1981, *Sol. Phys.*, **74**, 131
 Jiang, J., Isik, E., Cameron, R. H., Schmitt, D., & Schüssler, M. 2010, *ApJ*, **717**, 597
 Karak, B. B. 2010, *ApJ*, **724**, 1021
 Krivova, N. A., Balmaceda, L., & Solanki, S. K. 2007, *A&A*, **467**, 335
 Küker, M., Rüdiger, G., & Schultz, M. 2001, *A&A*, **374**, 301
 Lean, J. L. 2010, *Wiley Interdisciplinary Reviews: Climate Change*, **1**, 111
 Lean, J. L., Cook, J., Marquette, W., & Johannesson, A. 1998, *ApJ*, **492**, 390
 Lefebvre, S., et al. 2005, *Mem. Soc. Astron. Ital.*, **76**, 862
 Leighton, R. B. 1959, *ApJ*, **130**, 366
 Leighton, R. B. 1964, *ApJ*, **140**, 1547
 Mackay, D. H. 2003, *Sol. Phys.*, **213**, 173
 Makarov, V. I., & Sivaraman, K. R. 1989, *Sol. Phys.*, **119**, 35
 McIntosh, P. S. 1980, in *IAU Symp.* 91, *Solar and Interplanetary Dynamics*, ed. M. Dryer & E. Tandberg-Hanssen (Cambridge: Cambridge Univ. Press), **25**
 Muñoz-Jaramillo, A., Nandy, D., Martens, P. C. H., & Yeates, A. R. 2010, *ApJ*, **720**, L20
 Newkirk, G., Altschuler, M. D., & Harvey, J. 1968, in *IAU Symp.* 35, *Structure and Development of Solar Active Regions*, ed. K. O. Kiepenheuer (Cambridge: Cambridge Univ. Press), **379**
 Schrijver, C. J., De Rosa, M. L., & Title, A. M. 2002, *ApJ*, **577**, 1006
 Sheeley, N. R., Jr. 2008, *ApJ*, **680**, 1553
 Sheeley, N. R., Jr. 2010, in *ASP Conf. Ser.* 428, SOHO-23: Understanding a Peculiar Solar Minimum, ed. S. R. Cranmer, J. T. Hoeksema, & J. L. Kohl (San Francisco, CA: ASP), 3
 Sheeley, N. R., Jr., Walters, J. H., Wang, Y., & Howard, R. A. 1999, *J. Geophys. Res.*, **104**, 24739
 Sheeley, N. R., Jr., & Warren, H. P. 2006, *ApJ*, **641**, 611
 Shine, R. A. 1973, PhD thesis, Univ. Colorado at Boulder
 Title, A. 1966, *Selected Spectroheliograms* (Pasadena, CA: California Institute of Technology)
 Tlatov, A. G., Pevtsov, A. A., & Singh, J. 2009, *Sol. Phys.*, **255**, 239
 Ulrich, R. K., & Boyden, J. E. 2006, *Sol. Phys.*, **235**, 17
 Ulrich, R. K., Evans, S., Boyden, J. E., & Webster, L. 2002, *ApJS*, **139**, 259
 Wang, Y.-M., Lean, J., & Sheeley, N. R., Jr. 2002, *ApJ*, **577**, L53
 Wang, Y.-M., Robbrecht, E., & Sheeley, N. R. 2009, *ApJ*, **707**, 1372
 Wang, Y.-M., Sheeley, N. R., Jr., & Nash, A. G. 1991, *ApJ*, **383**, 431
 White, O. R., & Trotter, D. E. 1977, *ApJS*, **33**, 391